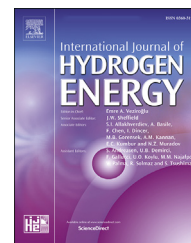


Available online at www.sciencedirect.com

ScienceDirect

journal homepage: www.elsevier.com/locate/he

Design methodology and thermal modelling of industrial scale reactor for solid state hydrogen storage

Nithin N. Raju, P. Muthukumar*, P. Vivek Selvan, K. Malleswararao

Department of Mechanical Engineering, Indian Institute of Technology, Guwahati, Assam 781039, India

ARTICLE INFO

Article history:

Received 8 January 2019

Received in revised form

19 May 2019

Accepted 26 May 2019

Available online 24 June 2019

Keywords:

Hydrogen storage

Metal hydride

Industrial scale reactor

3-D numerical modelling

Parametric investigation

ABSTRACT

In this study, a novel set of comprehensive arithmetic correlations has been proposed to design an industrial scale cylindrical reactor with embedded cooling tubes (ECT) for metal hydride (MH) based hydrogen storage and thermal management applications. Based on ASME standards, different nominal pipe sizes were imparted into a cylindrical reactor design with ECT to accommodate 50 kg of $\text{LaNi}_{4.7}\text{Al}_{0.3}$ alloy. A three dimensional numerical model has been developed using COMSOL Multiphysics 4.3a to predict the hydriding performance of designed reactors, which was further experimentally validated as well. At an absorption condition of 30 bar supply pressure and 298 K absorption temperature with 60 lpm volumetric HTF flow rate, 6 inch reactor with 99 ECT portrayed better heat transfer characteristics. From the parametric investigation, it is observed that the variation of supply pressure has predominant effect followed by the variation of the HTF flow rate on hydriding (absorption) kinetics of the device. However, the variation of absorption temperature has minuscule influence on the hydriding performance. At a supply condition of 30 bar and 298 K with water flow rate of 30 lpm, a hydrogen storage capacity (HSC) of 1.29 wt% was achieved within 2060 s.

© 2019 Hydrogen Energy Publications LLC. Published by Elsevier Ltd. All rights reserved.

Introduction

Energy is a primary need for sustenance of life. Its demand is growing rapidly over the years with the ever-increasing human population and thriving economy. Most of this demand is met from fossil fuels which are limited in nature. These fossil fuels are the primary cause of global warming that arises from various human activities such as extraction, processing, consumption and disposal of fossil fuels.

With the depletion of fossil fuels reserves and drastic rise in greenhouse gases emissions, there is an urgent need for

shifting the present hydrocarbon energy based economy towards clean and renewable energy based technologies, which generate near zero emission of greenhouse gases [1]. Hydrogen is such a fuel that contains an enormous amount of energy per unit mass, meets the above criteria and is indispensable to reach the world's energy demands and energy security. Most notable applications of hydrogen as an energy carrier are fuel cells, submarines, heat pumps, heat transformers, refrigerators and as fuel and reactant in welding, food industries, fertilizers and rocket fuels [2–6]. Storage of hydrogen is the most challenging task in Hydrogen Economy. Solid state hydrogen storage in the form of metal hydrides

* Corresponding author.

E-mail addresses: pmkumar@iitg.ac.in, pmkumariitg@gmail.com (P. Muthukumar).

<https://doi.org/10.1016/j.ijhydene.2019.05.193>

0360-3199/© 2019 Hydrogen Energy Publications LLC. Published by Elsevier Ltd. All rights reserved.

Nomenclature		Greek symbols	
Alphabets		ρ_o Effective density of MH [kg/m ³]	
b	Bed thickness [mm]	σ_h	Allowable stress [MPa]
c	Concentration, [H/M ratio]	ϕ_s	Slope factor
C_a	Absorption reaction rate constant [s ⁻¹]	ϕ_o	Slope constant
c_p	Specific heat capacity [J/kg-K]	ϕ	Hysteresis factor
D	Diameter [mm]	Subscripts	
E_a	Activation energy of absorption reaction [J/mol H ₂]	a	Angular
h	Outer radius of porous filter [mm]	abs	Absorption
HTF	Volumetric HTF flow rate [lpm]	e	Effective
K	Permeability [m ²]	end	Final
k	Thermal conductivity [W/m-K]	eq	Equilibrium
L	Length [mm]	eqi	Initial equilibrium
M	Molecular weight [g/mol]	f	Heat transfer fluid
m	Mass [kg]	g	Gas
N	Number of tubes	i	Inner
n	Number of moles [mol]	ini	Initial
P	Pressure [bar]	j	Positive integer
p	Pitch [mm]	max	Maximum
P_s	Supply pressure [bar]	MH	Metal hydride alloy
Q	Volumetric heat source [W/m ³]	o	Outer
R	Radius [mm]	op	Outer periphery of porous filter
R_u	Universal gas constant [J/mol-K]	R	Metal reactor
r	Radius of tubes [mm]	r	Radial
s	Number of stacks	re	Radial at end
T	Temperature [K]	rs	Radial near
t	At any given time [s]	s	Solid phase
t_{wall}	Thickness of tubes [mm]	t	At any given time
U	Overall heat transfer coefficient [W/m ² -K]	$vavg$	Volume averaged
\vec{u}	Velocity vector [m/s]	$grad$	Gradient
V	Volume [m ³]	Abbreviations	
Greek symbols		ECT	Embedded Cooling Tubes
ΔH	Enthalpy of absorption [J/mol H ₂]	HTF	Heat Transfer Fluid
ΔS	Entropy of absorption [J/mol H ₂ -K]	HSC	Hydrogen Storage Capacity
ε	Porosity	MH	Metal Hydride
ζ_a	Rate of mass of absorbed hydrogen [kg/m ³ -s]	MHHSR	Metal Hydride based Hydrogen Storage Reactor
μ	Dynamic viscosity [Pa-s]	PCT	Pressure-Concentration-Temperature
ρ	Density [kg/m ³]		
ρ_{ss}	Effective density of MH at saturation state [kg/m ³]		

(MH) offers several benefits over the other modes of storage such as compressed gas and liquid hydrogen using cryogenics at 20 K [7,8].

Over the last two decades, MHs have become the focus of research for hydrogen storage because of their ease of operation, safety, durability and economic niche. In addition, interaction of hydrogen with MH offers multiple thermal management applications for which MH can be synthesized addressing a specific application under a wide range of operating conditions. A rigorous research work is being carried out to implement metal hydrides in on-board applications (automotive and transportation industries), which demand reactors that are compact in design and lighter in mass [9]. Further, there is a minimal issue of leakage as hydrogen in MH is a solid solution. Because of the promising nature of metal hydrides in various thermal management applications, the research in field of MH has been paced up in this century.

Despite these appreciable features of the metal hydride based thermal management systems, a major limitation of these systems are their low gravimetric storage densities. For majority of applications such as in automotive industry, MHs with rapid reaction kinetics and high gravimetric storage density are required while they should be operable at near ambient conditions. It has been observed that the packing density as well as geometry of the MH container plays a vital role as well [10].

A recent review discusses the worldwide developmental status of better reactor configurations and heat transfer augmentation techniques wherein studies that are trying to scale the gap from available state of art systems to the system required for commercial applications [11]. Karagiorgis et al. [12] have developed a 6-stage novel metal hydride compressor that depicted stable operation in the range of 283–353 K. A specific productivity of 67.2 L_{H2}/kg h was attained by the

system wherein hydrogen supplied at 7 bar was compressed to 220 bar. Sharma and Kumar [13] have proposed a novel multi stage multi effect MH based sorption system that can be operated simultaneously for heat pumping, heat transformation and cooling application. They utilized 4 AB₅ type alloys of 2.75 kg and the system was able to produce 3337 kJ cooling, 3243 kJ high grade heat and 5726 kJ low grade heat with overall COP of 2.22 with a cycle time of 64 min.

Bellosta von Colbe et al. [14] have reviewed in detail the achievements and perspectives of hydrogen storage and compression applications. Modular MH based thermal management applications are simpler in construction and have been well established. Ingeniously combining these established MH based systems, an amalgamated polygeneration system can be proposed. Bhogilla et al. [15] developed a totalized hydrogen energy utilization system with a maximum combined efficiency of 66%. The primary component of this system is a unitized reversible fuel cell with a maximum efficiency of 53%. A compact metal hydride based hydrogen storage tank for fuel cell utility vehicles was developed by Lototskyy et al. [16]. The tank was able to provide hydrogen supply for more than 2 h at a flow rate of 120 NL/min for a fuel cell stack being operated at 11 kWe. At a supply of 100–150 bar, the refuelling time for the tank was about 15–20 min at a temperature of 293 K.

Although extensive numerical and experimental research works have been published on performance investigations of lab-scale reactors (capacity up to 5 kg alloy mass) [17–24], there is a need for intense research on industrial scale models (about 30–100 kg alloy mass) with emphasis on practical challenges/thermal management issues. Nakano et al. [25] have developed a hydrogen storage tank containing 50 kg of MmNi₅ alloy embedded with a double coil type heat exchanger. At an absorption rate of 11.8 NL/min, 6350 NL of hydrogen was absorbed from initial composition (H/M) of 0.18. The same amount was desorbed from composition (H/M) of 1.0 at a desorption rate of 8.1 NL/min. Tarasov et al. [26] developed a metal hydride based hydrogen compressor which contained 30 kg of LaNi₅ in the first stage while 24 kg of La_{0.5}Ce_{0.5}Ni₅ in the second stage. However, the factor to note in this study was that the storage module was a bundle of tubular containers holding a part load of chosen MH alloy. The overall system was able to compress hydrogen from 3.5 atm to 150 atm in two stages while operating between temperature ranges of 288–293 K and 423–433 K. Using a four module system containing modified sodium alanate, Johnson et al. [27] were able to store 3 kg of hydrogen which corresponds to 4.0 wt% of hydrogen uptake. Similar to prior study, they have developed a storage module comprising of 12 tubes, each filled with 1.79 kg of alloy.

For compact reactor designing with large scale MH alloy capacity, there is a lack of systematic approach considering the heat transfer augmentations, parasitic thermal mass of reactor, economy and fabrication constraints of industrial scale metal hydride based hydrogen storage reactors (MHHSR). Extensive researches have been carried out to improve absorption and desorption kinetics [28]. In general, the effective thermal conductivity of hydride bed is low [29] and this significantly affects the absorption/desorption performance of MHHSR. Aluminium foam has been employed in

MHHSR to enhance the heat transfer between MH bed and HTF and thereby improving the performance of MHHSR [30–33]. A sensitivity analysis conducted on factors influencing MH absorption kinetics showed that thermal conductivity and pressure are crucial. Krokos et al. [34] developed a 3-D model of multi-tubular MHHSR containing LaNi₅ and proposed an optimum reactor geometry which has minimum absorption time. Raju and Khaitan [35,36] presented a 24 cooling tube heat exchanger model with aluminium fins to study the absorption/desorption characteristics of a MHHSR coupled with a fuel cell for a small scale wind hybrid system. Muthukumar et al. [37] presented a 2-D numerical model of MHHSR with embedded cooling tubes (ECT) for predicting the reaction kinetics at various absorption conditions. Anbarasu et al. [38] developed a 2-D thermal model to predict the performance of MHHSR by varying the number of ECT from 24 to 70 and further they extended their study to 3-D thermal modelling of MHHSR with 60 ECT. They had varied the ECT geometrically by considering angular pitch between ECT in each stack and reported that the rapid absorption was found at 35 bar supply with effective thermal conductivity of 2.5 W/m-K for 60 ECT reactor.

Different heat exchanger designs such as straight tube heat exchanger, coiled heat exchanger, transverse fin and cooling jacket heat exchanger have been proposed [39–43]. As the effective thermal conductivity of the MH bed is low, ensuring an optimum thickness of the hydride bed available for each heat transfer surface enhances the heat transfer rate and results in improved hydriding or dehydriding rates.

Mohan et al. [18] had proposed an evenly distributed reactor with embedded cooling tubes and filters in order to increase the number of hydrogen absorption reaction nuclei. Recently, a heat exchanger with radial circular perforated copper fins for holding 1 kg of LaNi₅ alloy was designed by Singh et al. [29]. They observed a charging time of 18 min at supply condition of 15 bar and 298 K with HTF velocity of 1 m/s. The cylindrical reactor with ECT have got special attention in the design of MH reactor based system due to their simple and efficient heat exchanger design [44–46].

However, there is a profound lack of an adaptable strategy when it comes to the design of embedded tube reactors, especially for industrial applications. Some of the devised approaches are too complex and demand higher manufacturing cost. Hence, a novel set of comprehensive arithmetic correlations has been developed as a strategy to select the reactor shell size for required alloy capacity and design them with ECT distribution such that bed thickness at each cooling surface is uniform. This is done while balancing the design against resulting parasitic thermal mass of empty reactor. Utilizing this strategy, reactor design of different scale and multiple avenues of applications can be addressed.

Secondary focus of this study is to determine the feasibility of large scale MH reactors for industrial scale storage and utilization of hydrogen. This is addressed through the parametric investigation of selected reactor configuration at various operating conditions. A commercial supply cylinder of 47 lit capacity at a pressure of 150 bar contains about 425 g of hydrogen. This amounts to a storage capacity of 0.85 wt% for 50 kg of LaNi_{4.7}Al_{0.3} alloy system. Considering absorption of this volume, the system should be able to attain a storage

capacity of 1 wt% within 1000 s when hydrogen is supplied at 20 bar and HTF is at an ambient temperature. The above conditions has been described considering operational feasibility of this system in an industry.

Design methodology

Various reactor geometries have been detailed and their suitability for specific application have been discussed [47,48]. In a tubular or cylindrical geometry, hydrogen flow within reactor takes place through a central artery while MH alloy is packed in the annular space between the artery and the wall. Tubular configuration provides good sealing and high bearing pressure. They demonstrate effective heat and mass transfer if fabricated by thin tubes [47]. The geometry allows for a uniform distribution of the mechanical stresses that results from cyclic pressurization [48]. Further heat transfer enhancement can be achieved by implementing embedded heat exchangers within the bed. Tubular reactors are easier to manufacture as standardized tubing are available. Comparatively, disc reactors have limited MH alloy capacity, while chamber type reactors are not suitable for compact and mobile applications as they are bulkier. Hence, tubular geometry has been chosen for present study. Considering hydrogen permeability in metals and prerequisite strength for high pressure applications, stainless steel SS316 is chosen as reactor material. A porous filter made of sintered SS316 material with a pore size of 2 μm having an outer diameter of 14 mm and thickness of 2 mm is centrally placed as shown in Fig. 1. Hydrogen gas is supplied through the porous filter which facilitates uniform distribution of gas throughout the length of reactor during absorption and also filters MH particles from being carried away by the H_2 gas. ECT are made of SS316 with an outer diameter of 6.35 mm and thickness of 0.89 mm. As represented in Fig. 1, they are distributed within

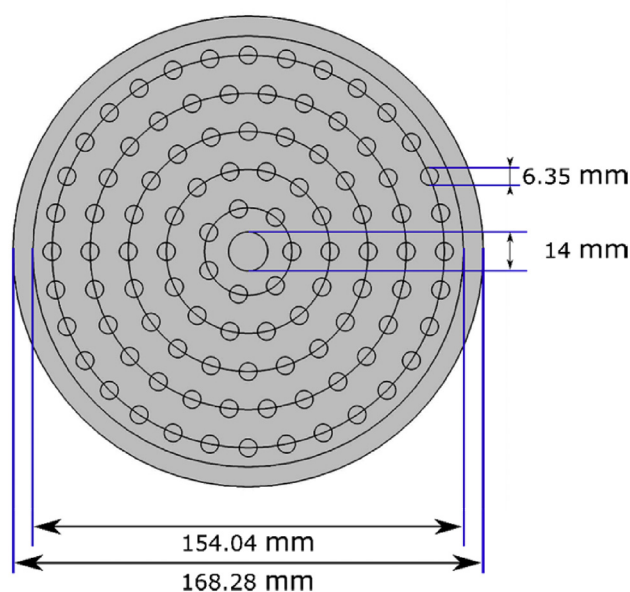


Fig. 1 – Cross sectional schematic view of reactor with ECT using 6 inch nominal diameter cylindrical shell.

the reactor shell in a layered formation named as stacks. The radial locations and number of tubes in each stack are deduced based on the developed correlations. The selection of suitable pipe for cylindrical reactor shell using ASME standard has been discussed in supplementary material.

In present study, bed thickness (b) is considered as the minimum distance between two cooling interfaces since the design focuses on the heat transfer between bed and HTF in this region. Various components of design correlations are represented in Fig. 2, which includes radius of porous filter (h), inner radius of cylindrical shell (R_i), radial pitch (p_r) and angular pitch (p_a) between ECT. Further, ' p_{rs} ' represents radial pitch between supply porous filter and ECT of first stack while ' p_{re} ' represents radial pitch between ECT of last stack and inner periphery of reactor shell. As the bed thickness should be uniform between ECT both in angular and radial direction,

$$p_r = p_a = b \quad (C1)$$

Since, the periphery of reactor shell and supply filter are considered to be adiabatic, only the ECT interfaces provide heat transfer. Hence, ' p_{re} ' is estimated as half of bed thickness,

$$p_{re} = 0.5 * b \quad (C2)$$

Placement of first stack around supply porous filter is difficult as it involves welding of ECT and supply porous filter onto end flange plates, which would be discussed in section Validation. Based on prior design and fabrication experience, a factor of 1.5 is considered for estimation of ' p_{rs} ' as,

$$p_{rs} = 1.5 * p_{re} \quad (C3)$$

Based on these considerations, a relation between bed thickness (b) and number of stacks (s) is devised using ' R_i ' from Fig. 1 as,

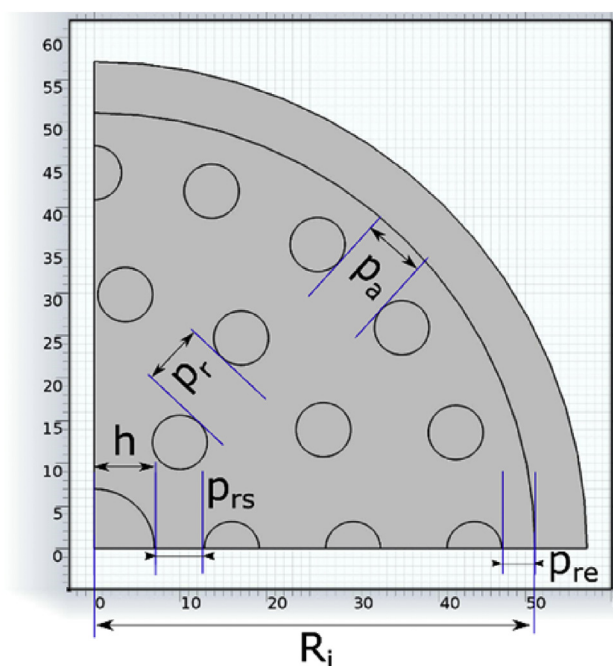


Fig. 2 – Sectional view of typical reactor with ECT representing components of design correlation.

$$R_i = h + s*(2r_o) + (s-1)p_r + p_{re} + p_{rs} \quad (C4)$$

where ' r_o ' denotes outer radius of ECT. Using correlations C1, C2 and C3, C4 is rewritten as,

$$R_i = h + s*(2r_o) + (s-1)b + 0.5*b + 0.75*b$$

which essentially provides the relation between ' s ' and ' b ' as,

$$b = \frac{R_i - h - s*(2r_o)}{(s + 0.25)} \quad (C5)$$

Value of bed thickness (b) is estimated for fixed ' R_i ', ' h ' and ' r_o ' values while varying the number of stacks (s). From reported literatures, it is observed that higher bed thickness leads to poor conductive heat transfer within MH bed. However, decreasing it to a very low value leads to a case of over-optimization wherein the parasitic thermal mass of resulting design will be too high. Taking input from the reported effect of bed thickness on reaction kinetics of MH [17,45–51], value of ' b ' has been ensured between 5 and 10 mm while varying ' s ' among positive integers. To better explain this strategy, the bed thickness and ratio of empty reactor mass to 50 kg alloy mass are estimated for different ' s ' values considering 6 inch and 4 inch nominal size shells, as represented in Fig. 3.

It is observed from Fig. 3, that in case of 6 inch nominal size reactor, 3 and 4 stack structures resulted in respective bed thickness of 15.68 mm and 10.5 mm which are quite adverse for heat transfer. Though the corresponding bed thickness are 5.11 mm and 3.53 mm for 6 and 7 stack structure, the resultant reactor mass are respectively 1 and 1.26 times than that of alloy mass, which would result in more parasitic thermal mass. Hence, 5 stack structure having 7.29 mm bed thickness with mass ratio of 0.803 is chosen. From Fig. 3, it is also inferred that the 4 inch model having 3 stack structure with bed thickness of 7.72 mm is ideal. Analysis of 5 inch and 8 inch reactor shells resulted in 4 and 6 stack structures, respectively.

Considering the pitch and radius of ECT, radial location of first stack (R_1) and j^{th} stack (R_j) are deduced from ' b ' and ' s ' values as,

$$R_1 = h + p_{rs} + r_o \quad (C6)$$

$$R_j = R_{j-1} + p_r + 2*r_o \quad (C7)$$

where, ' j ' is varied here from 2 to ' s '. From location of j^{th} stack, number of ECT in j^{th} stack (N_j) is estimated as,

$$N_j = \frac{2\pi*R_j}{2*r_o + p_r} \quad (C8)$$

where, ' j ' is varied here from 1 to ' s '. The resulting ' N_j ' is rounded off to next positive integer as it represents number of ECT. Summation of ECT in each stack lead to total number of ECT (N_{total}) as,

$$N_{total} = \sum_{j=1}^s N_j \quad (C9)$$

Considering 50 kg of alloy mass (m_{MH}) and effective density of MH alloy at saturated state (ρ_{ss}), required volume for MH alloy storage is estimated as,

$$V_{MH} = 1.2 * \frac{m_{MH}}{\rho_{ss}} \quad (C10)$$

wherein a safety factor of 1.2 is considered to account for volumetric expansion during absorption of MH. Required length of reactor (L) is estimated by considering required volume and available cross sectional area for MH storage as given by,

$$L = \frac{V_{MH}}{\pi(R_i^2 - N_{total}*r_o^2 - h^2)} \quad (C11)$$

Hence, mass of empty reactor (m_R) is estimated as,

$$m_R = \rho_R \pi L [(R_o^2 - R_i^2) + N_{total}*(r_o^2 - r_i^2)] \quad (C12)$$

where ' ρ_R ' denotes density of SS316, ' R_o ' and ' r_i ' respectively denote outer radius of reactor shell and inner radius of ECT. Determining the ratio of empty reactor metal mass to alloy mass of 50 kg (m_R/m_{MH}) is a crucial factor for reactor design. Based on these correlations, reactors of 4 inch, 5 inch, 6 inch and 8 inch nominal pipe sizes are designed as detailed in Table 1. It is interesting to note that the bed thickness of all these designs ranged between 7.29 mm and 9 mm only. The designed assembly of cylindrical shell with supply porous filter and ECT arrangement is collectively termed as principal reactor chamber. In the physical model, end flange plates having thickness 1.5 times that of reactor shell thickness are welded onto both ends of principal chamber. Supply tube is welded onto porous filter while auxiliary fluid flow chambers are welded onto the end flange plates. They act as HTF collection chambers at inlet and outlet of the ECT. Based on the nominal pipe sizes and total number of ECT, the reactors are respectively labelled as RI_4in_40ECT, RII_5in_67ECT, RIII_6in_99ECT and RIV_8in_136ECT. Only the principal chamber of the reactor designs are considered for the numerical modelling.

Numerical modelling

Three dimensional numerical model using COMSOL Multiphysics 4.3a employing the designed reactor is developed

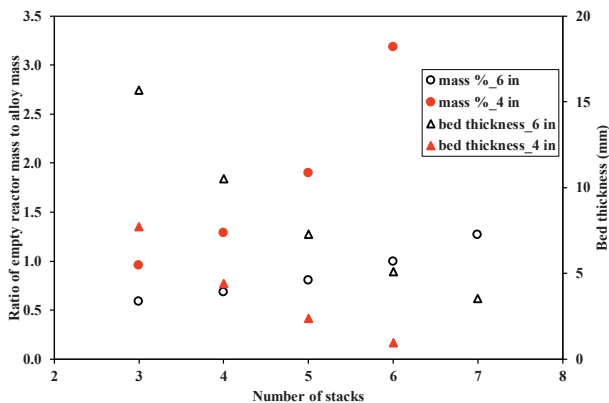


Fig. 3 – Influence of number of stacks on bed thickness and ratio of empty reactor mass to alloy mass.

Table 1 – Evaluated design parameters based on developed correlations for shells of different nominal pipe size.

Nominal pipe size (inch)	Outer diameter (mm)	Thickness (mm)	Internal diameter (mm)	Radial location of each stack (mm)	No. of tubes at each stack	Total no. of tubes	Reactor length [mm]	Mass of empty reactor [kg]	Mass ratio (m_R/m_{MH})
4	114.30	6.02	102.26	15.96	7	40	2262.69	47.73	0.955
				30.03	13				
				44.10	20				
5	141.30	6.55	128.19	15.77	7	67	1445.47	43.40	0.868
				29.58	14				
				43.39	20				
6	168.28	7.12	154.05	57.20	26	99	1001.27	40.15	0.803
				15.64	7				
				28.28	14				
8	219.08	8.18	202.72	42.92	20	136	552.53	32.65	0.653
				56.56	26				
				70.20	32				
				16.93	7				
				32.28	13				
				47.63	20				
				62.98	26				
				78.33	32				
				93.68	38				

considering 50 kg of $\text{LaNi}_{4.7}\text{Al}_{0.3}$ alloy. In this numerical study, the thickness of ECT is neglected. As the reactor design is symmetric along the radial axis ($Y-Y'$), the numerical simulation is performed considering longitudinal half sectional model so as to reduce the computational expense. Schematic of half sectional numerical model of RIII_6in_99ECT reactor is represented in Fig. 4. Water is considered as HTF for this study.

Assumptions

Gas transport phenomenon within MH bed, combined heat and mass transfer characteristics arising from absorption reaction, variable wall convective boundary at ECT interface and variation of hydrogen concentration within bed are considered in this study with following assumptions:

- > Ideal gas consideration for hydrogen gas.

- > Local thermal equilibrium between the gas and metal hydride bed is valid.
- > The effect of radiative heat transfer is neglected.
- > The solid phase is isotropic and has uniform porosity.
- > The centrally placed porous filter is adiabatic and allows only hydrogen to pass through.
- > Hydrogen gas is supplied to the reactor at a known constant pressure.
- > Thermal conductivity and specific heat capacity of chosen alloy are independent of pressure, temperature and concentration of hydrogen.
- > The reactor shell is assumed to be well insulated so that there is no heat transfer with surroundings.

Governing equations

Following governing equations are utilised to model and simulate the system.

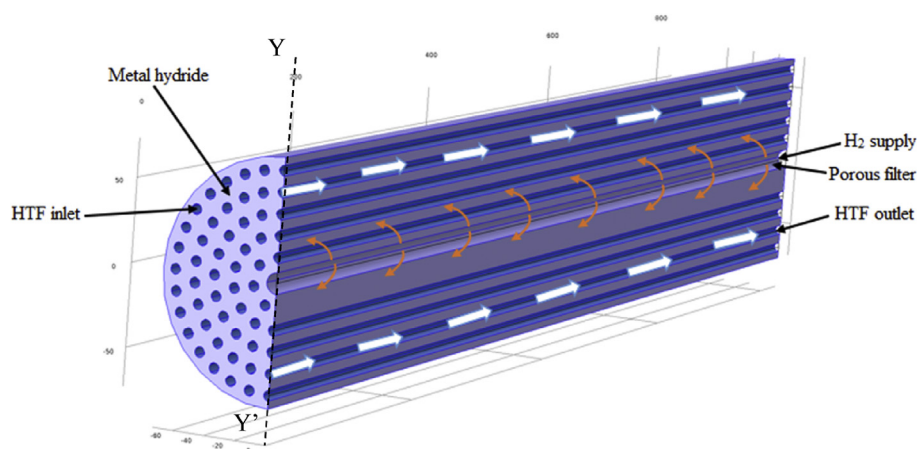


Fig. 4 – Schematic view of typical ECT reactor implemented in numerical modelling (3-D half sectional).

Reaction rate

The rate of mass of hydrogen absorbed (ζ_a) per unit volume per unit time by the MH is given as [52],

$$\zeta_a = C_a \exp\left(-\frac{E_a}{R_u T}\right) \ln\left(\frac{P_s}{P_{eq}}\right) (\rho_{ss} - \rho_t) \quad (1)$$

where ' C_a ' denotes reaction rate constant, ' E_a ' is activation energy, ' R_u ' is universal gas constant, ' P_s ' and ' P_{eq} ' respectively denote supply pressure and equilibrium pressure of MH alloy and ' ρ_t ' denotes the density of MH alloy at any time 't' during the absorption.

Mass balance

Considering the amount of hydrogen absorbed as the sink term, the continuity equation for hydrogen gas is formulated as [37],

$$\varepsilon \frac{\partial \rho_g}{\partial t} + \nabla \cdot (\rho_g \vec{u}) = -\zeta_a \quad (2)$$

where ' ρ_g ' denotes the density of hydrogen gas within the bed, ' \vec{u} ' is the velocity vector and ' ε ' represents porosity. Density of hydrogen gas (ρ_g) can be evaluated from ideal gas equation,

$$\rho_g = \frac{P_g M_g}{R_u T} \quad (3)$$

where ' P_g ' is the gas pressure and ' T ' is the temperature within MH bed while ' M_g ' is the molecular weight of gaseous hydrogen and ' R_u ' is the universal gas constant. For solid phase where amount of hydrogen absorbed is source term, mass balance equation is considered as,

$$(1 - \varepsilon) \frac{\partial \rho_s}{\partial t} = \zeta_a \quad (4)$$

Momentum balance

Velocity of hydrogen flow inside MH bed (\vec{u}) is modelled considering pressure gradient using Darcy's Law as given by,

$$\vec{u} = -\left(\frac{K}{\mu_g}\right) \nabla P \quad (5)$$

where ' K ' is the permeability of the MH bed and ' μ_g ' is the dynamic viscosity of hydrogen gas.

Energy balance

Considering local thermal equilibrium between the MH bed and hydrogen gas, a combined energy equation is written as [37],

$$(\rho c_p)_e \frac{\partial T}{\partial t} + (\rho c_p)_g (\vec{u} \cdot \nabla T) = k_e \nabla^2 T + Q \quad (6)$$

where ' T ' represents temperature and ' Q ' is the heat source term given by [53],

$$Q = \zeta_a \left(\frac{\Delta H}{M_g} - (c_{pg} - c_{ps}) T \right) \quad (7)$$

where ' ΔH ' is the enthalpy of absorption. In the energy balance equation, effective heat capacity ($(\rho c_p)_e$) is given by,

$$(\rho c_p)_e = (1 - \varepsilon)(\rho c_p)_s + \varepsilon(\rho c_p)_g \quad (8)$$

where ' $(\rho c_p)_g$ ' denotes heat capacity of gas phase, while ' $(\rho c_p)_s$ '

represents heat capacity of solid phase. Similarly, the effective thermal conductivity is obtained as,

$$k_e = (1 - \varepsilon)k_s + \varepsilon k_g \quad (9)$$

In case of HTF, energy equation is formulated as,

$$(\rho c_p)_f \frac{\partial T_f}{\partial t} + (\rho c_p)_f (\vec{u}_f \cdot \nabla T_f) = k_f \nabla^2 T_f \quad (10)$$

where ' k_f ' is the thermal conductivity of the HTF, and ' \vec{u}_f ' is the velocity vector.

van't Hoff equation

During the absorption process, the equilibrium pressure inside the MH bed is calculated using modified van't Hoff equation [54],

$$\frac{P_{eq}}{P_0} = \exp\left[\frac{\Delta S}{R_u} - \frac{\Delta H}{R_u T} + (\varphi_s + \varphi_o) \times \tan\left(\pi\left(\frac{c_t}{c_{end}} - \frac{1}{2}\right)\right) + \frac{\varphi}{2}\right] \quad (11)$$

where ' P_0 ' denotes atmospheric pressure, ' ΔS ' is the entropy of absorption, while ' φ_s ', ' φ_o ' and ' φ ' respectively denote slope factor, slope constant and hysteresis factor. Concentration is the ratio of number of hydrogen atoms absorbed over the total number of metal atoms present per mole of alloy. Concentration at any given time 't' is given by ' c_t ' while final concentration is represented as ' c_{end} '.

Hydrogen storage capacity

Considering mass (m_{MH}) and molecular weight (M_{MH}) of MH alloy, number of moles of hydrogen absorbed (n_g) is estimated as [37],

$$n_g = \frac{m_{MH} A_{MH} (c_t - c_{ini})}{2 M_{MH}} \quad (12)$$

where ' c_{ini} ' represents initial concentration while ' A_{MH} ' denotes number of metal atoms per mole of alloy. Resultant mass of hydrogen absorbed is evaluated as,

$$m_g = n_g M_g \quad (13)$$

The hydrogen storage capacity (HSC) is the mass of hydrogen absorbed (m_g) with respect to total mass of MH alloy (m_{MH}) at any given time 't', often expressed in terms of weight percentage (wt%). This is obtained using Eqs. (12) and (13) as,

$$HSC(\text{wt}\%) = \frac{m_g}{m_{MH}} \times 100\% = \frac{A_{MH} M_g (c_t - c_{ini})}{2 M_{MH}} \times 100\% \quad (14)$$

while maximum or total HSC is given by,

$$\text{Maximum HSC (wt}\%) = \frac{A_{MH} M_g (c_{end} - c_{ini})}{2 M_{MH}} \times 100\% \quad (15)$$

Initial and boundary conditions

Initial conditions

Initially at time 't' = 0, temperature of bed and HTF are considered to be uniform throughout model at the ambient temperature (T_0):

$$T(t=0) = T_f(t=0) = T_0 \quad (16)$$

Pressure and MH density are supposed to be uniform throughout the model, respectively as:

$$\rho_s(t=0) = \rho_0 \quad (17)$$

$$P(t=0) = P_{eqi} \quad (18)$$

where ' P_{eqi} ' is the initial equilibrium pressure of the bed which is the function of initial concentration and temperature, while ' ρ_0 ' is the effective density of MH at initial state.

Boundary conditions

At ECT interface, convective boundary condition at each cooling tube is given by,

$$-k_e \frac{\partial T}{\partial r} \Big|_{r=r_o} = U[T - T_f] \quad (19)$$

where ' r_o ' is the outer radius of the ECT while ' U ' is the overall heat transfer coefficient. The porous filter is assumed to be adiabatic while the gas pressure at the periphery of filter is equal to supply pressure (P_s):

$$P_g \Big|_{r=r_{op}} = P_s \quad (20)$$

$$\frac{\partial T}{\partial r} \Big|_{r=r_{op}} = 0 \quad (21)$$

The outer periphery of the metal hydride container is assumed to be adiabatic:

$$\frac{\partial T}{\partial r} \Big|_{r=R_o} = 0 \quad (22)$$

Inlet of ECT is specified to be at absorption temperature (T_{abs}). For HTF domain,

$$T_f \Big|_{z=L} = T_{abs} \quad (23)$$

Grid independent test

To analyse the effect of grid size variation on the accuracy of numerical prediction, a grid independent test is conducted on volume averaged bed temperature variation during the absorption reaction of RIII_6in_99ECT reactor model containing 50 kg of $\text{LaNi}_{4.7}\text{Al}_{0.3}$. The thermo-physical properties of $\text{LaNi}_{4.7}\text{Al}_{0.3}$ which are taken from reported literature [49,55] along with properties of hydrogen gas and constants used in this modelling are listed in Table 2.

For this analysis, models of different grid sizes are generated and their details along with duration of computation are presented in Table 3. The observed result of grid independent analysis is portrayed in Fig. 5. It can be observed that for a given absorption condition of 30 bar, 298 K with HTF flow rate of 45 lpm, there is a significant change in the bed temperature variation and in computation time when the number of elements is increased from 6,89,929 (grid 1) to 8,52,989 (grid 2). For 14.9% increase in computation duration, nearly 5% reduction is witnessed in absorption time.

When grid size is increased further to 10,53,580 (grid 3), 19% increase in computation duration resulted in 2% refinement in results. Further refinement is not perceived when the number of elements is increased beyond grid 3 to grid 4 with 11,77,945 elements. Hence, further mesh improvement beyond grid 4 is

Table 2 – Thermophysical properties of $\text{LaNi}_{4.7}\text{Al}_{0.3}$ and hydrogen and constants [49,55].

Parameters	Value
Properties of $\text{LaNi}_{4.7}\text{Al}_{0.3}$	
Specific heat capacity of metal (c_{ps})	420 J/kg-K
Thermal conductivity of MH (k_s)	1.3 W/m-K
Porosity (ϵ)	0.5
Effective density of MH (ρ_0)	3720 kg/m ³
Effective density of MH at saturation state (ρ_{ss})	3770 kg/m ³
Activation energy (E_a)	33900 J/mol H ₂
Reaction entropy (ΔS)	107.4 J/mol H ₂ -K
Reaction enthalpy (ΔH)	33820 J/mol H ₂
Molecular weight (M_{MH})	422.9 g/mol
Properties of hydrogen	
Thermal conductivity (k_g)	0.1272 W/m-K
Specific heat capacity (c_{pg})	14,283 J/kg-K
Density (ρ_g)	0.0838 kg/m ³
Molecular weight (M_g)	2.016 g/mol
Constants used	
Universal gas constant (R_u)	8.314 J/mol-K
Reaction constant (C_a)	250 s ⁻¹
Slope factor (ϕ_s)	0.3
Slope constant (ϕ_o)	0.005
Hysteresis factor (ϕ)	0.098

not performed and mesh properties of grid 3 is selected for the computational study.

Validation

To validate the numerical results, fabricated model of RIII_6in_99ECT was filled with 40 kg of $\text{LaNi}_{4.7}\text{Al}_{0.3}$. The length of the model was shortened to 700 mm, as the filled alloy mass was 40 kg. The physical model of reactor is represented in Fig. 6 wherein the principal chamber (C) is of RIII_6in_99ECT configuration based on the design methodology. As per the design, the SS316 cylindrical shell was of 168.28 mm in outer diameter and 7.12 mm in thickness. A sintered SS316 tube having an outer diameter of 14 mm and thickness of 2 mm had been centrally placed in the principle chamber. In a five stack structure around the sintered tube, 99 ECT had been distributed as per configuration. The tubes are of SS316 having an outer diameter of 6.35 mm and thickness of 0.89 mm. The shell and the tubes were welded on both ends to 10 mm thick circular plates which are termed as end flange plates. On both outside ends, auxiliary fluid flow chambers (A) were welded onto the end flange plates as shown in Fig. 6. Hydrogen supply tubes (D) were welded onto end flange plates such that the supplied hydrogen flows directly through the porous tube inside reactor.

Table 3 – Grid elements and time taken for absorption process.

Name	Number of elements	Computation duration	Absorption time
grid 1	6,89,929	27966 s	2640 s
grid 2	8,52,989	32137 s	2510 s
grid 3	10,53,580	38229 s	2470 s
grid 4	11,77,945	42639 s	2460 s

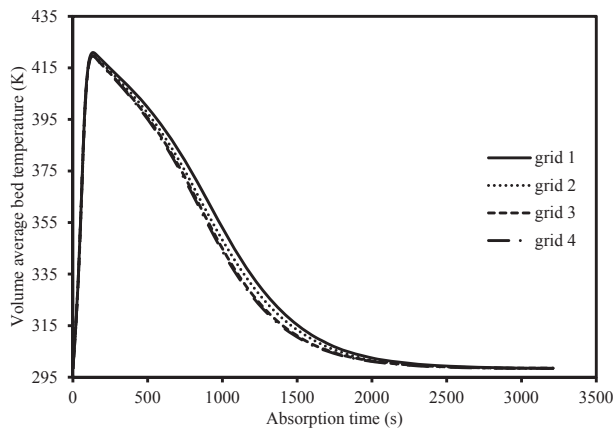


Fig. 5 – Volume average bed temperature variation of RIIL_6in_99ECT for different grid sizes.

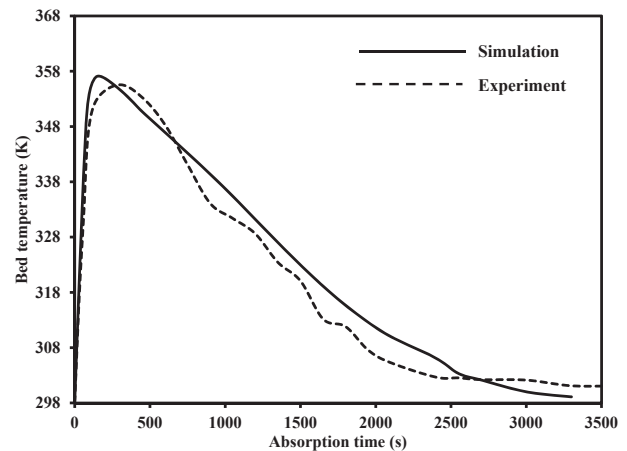


Fig. 7 – Validation of bed temperature.

The temperature at various locations of the hydride bed was sensed using K-type thermocouples (B). The thermocouples were axially located with an interval of 100 mm between them while their sensing ends were at a depth of 45 mm from outer periphery. The first thermocouple was axially located at a distance of 100 mm from the inlet end flange plate. The experiment was conducted at supply pressure of 10 bar and absorption temperature of 298 K with 30 lpm water flow rate. Along with the described reactor, the experimental setup consisted of Coriolis flow meter, pressure gauges and turbine type flow meter for HTF. The measurement accuracy of K-type thermocouples was estimated to be ± 0.5 K, while the uncertainty in HTF flow rate was estimated as $\pm 1.67\%$. The numerical model of RIIL_6in_99ECT reactor with 40 kg MH was simulated at the same absorption condition. The hydride bed temperature of the numerical model was evaluated at same locations corresponding to the thermocouple sensing ends in the physical model. The arithmetic average bed temperature was evaluated from both experimental investigation and numerical simulation as compared in Fig. 7, and a good agreement is observed between them.

The deviation between the predicted and experimental values of bed temperature is represented in Fig. 8. The average bed temperature was predicted to be maximum at 359 K in numerical simulation, while it was at 355.7 K in experimental

analysis. There was a slight delay in experimental average bed temperature attaining its peak value compared to the numerical prediction. This deviation was observed during the initial stage of absorption reaction and can be attributed to non-uniform porosity of actual MH bed. However, deviation was well within $\pm 4\%$ when the predicted average bed temperature was compared with corresponding experimental data.

The predicted HTF outlet temperature was compared with outlet HTF temperature of experimental analysis as shown in Fig. 9. The maximum temperature of HTF was predicted to be 307.7 K whereas in experiment, it was 307.8 K after a delay of about 60 s. HTF outlet temperature of experiment attained 300 K as opposed to 298 K in case of predicted value of numerical model, due to slight increment in HTF inlet temperature during experiment. This overall analysis corroborates validity of developed numerical model.

Results and discussions

The influence of different reactor configurations on the hydriding characteristics of MHHSR is discussed in this section. The best reactor design among different configurations is selected based on its hydriding performance for further

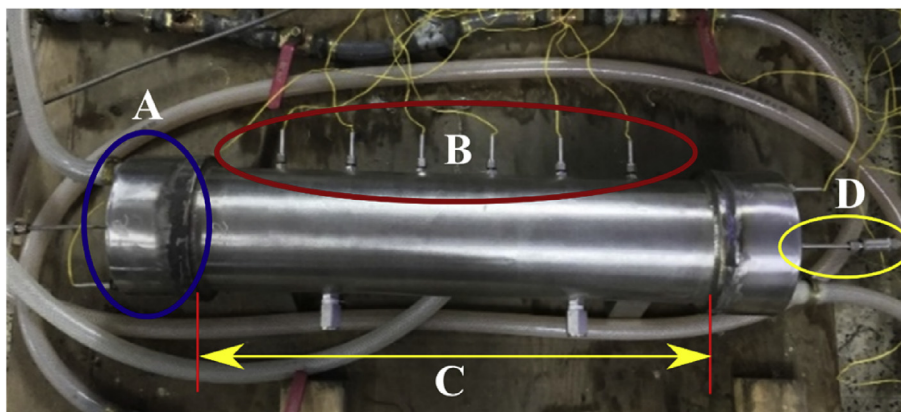


Fig. 6 – Physical model of RIIL_6in_99ECT reactor.

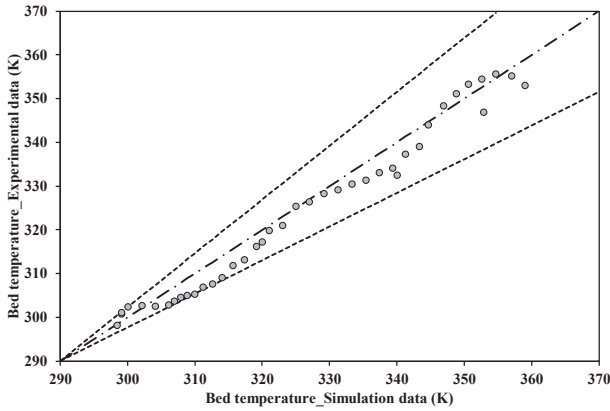


Fig. 8 – Comparison between the simulation and experimental data of arithmetic average bed temperature.

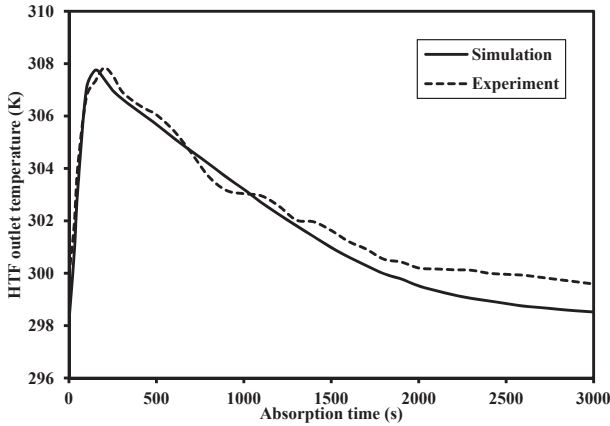


Fig. 9 – Validation of HTF outlet temperature.

parametric analysis wherein the effect of hydrogen supply pressure, absorption temperature and HTF flow rate on absorption rate of MH are analysed.

Effect of reactor configuration

Numerical models of the different reactor configurations namely RI_4in_40ECT, RII_5in_67ECT, RIII_6in_99ECT and RIV_8in_136ECT are developed for 50 kg of $\text{LaNi}_{4.7}\text{Al}_{0.3}$ and simulated at an absorption condition of 30 bar and 298 K with water flow rate of 60 lpm. The observed variation of volume average bed temperature, HSC and HTF outlet temperature are discussed in detail.

Variation of volume average bed temperature

The effect of reactor configuration on the variation of the volume average bed temperature (T_{avg}) during absorption is represented in Fig. 10. As the mass of alloy is same in all models, the dimensions and ECT arrangement of each reactor configuration plays a crucial role on hydriding rate. Initially, the absorption is rapid due to substantial pressure gradient between equilibrium bed pressure and supply pressure. This leads to rapid evolution of exothermic heat that causes

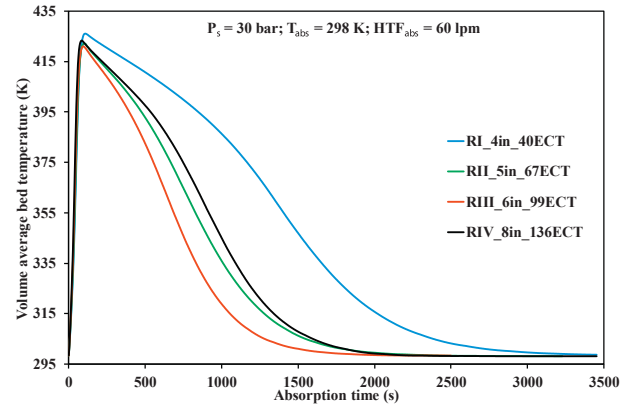


Fig. 10 – Effect of reactor geometry on volume average bed temperature variation.

sudden increase in bed temperature. This mechanism of interaction is same for all configurations which is reflected by their peak value of T_{avg} . The evolving heat of absorption is removed by HTF wherein the arrangement of ECT influences the interaction. Among the reactor configurations, RIII_6in_99ECT exhibits better heat transfer characteristics, while hydriding of RI_4in_40ECT is comparatively slow due to its length of 2262.7 mm. In RI_4in_40ECT, temperature of HTF flowing throughout reactor length increases to such an extent that the temperature gradient between bed and HTF reduced which affects the amount of heat removed from bed. T_{avg} drops to 300 K, from peak value of 426 K within 2778 s for RI_4in_40ECT while the value drops from 422.6 K within 1497 s for RIII_6in_99ECT, which amounts to 46% reduction in time. Owing to their designs, both RII_5in_67ECT and RIV_8in_136ECT depict similar performance while requiring 20.1% more time than RIII_6in_99ECT for dropping to 300 K.

Variation of hydrogen storage capacity (HSC)

The variation of HSC is similar to that of T_{avg} variation, as the rate of heat removal dictates the rate of hydrogen absorption. Reactor with higher heat transfer rate depicts better hydriding rate as can be observed from Fig. 11. Total HSC of 1.29 wt% is achieved by all configurations, while 50% of total HSC is achieved within 140 s by RIII_6in_99ECT model. For 80% of absorption amounting to HSC of 1.03 wt%, a duration of just 430 s is required by this model. Comparatively, RII_5in_67ECT and RIV_8in_136ECT models require 17.5% and 22.8% more time respectively to achieve HSC of 1.03 wt%. This is due to the fact that RII_5in_67ECT is longer than RIII_6in_99ECT which leads to higher increase in HTF temperature resulting in lesser temperature gradient and thereby leading to poor heat transfer. In case of RIV_8in_136ECT, it is broader than RIII_6in_99ECT and this causes a slight delay in complete absorption of bed near periphery region of model. Due to its sizable length, RI_4in_40ECT requires 82.5% more duration than RIII_6in_99ECT to achieve HSC of 1.03 wt%.

Variation of HTF outlet temperature

As discussed, the HTF outlet temperature of RI_4in_40ECT is higher than the other models leading to slower heat removal rate. From Fig. 12, it is observed that the HTF outlet

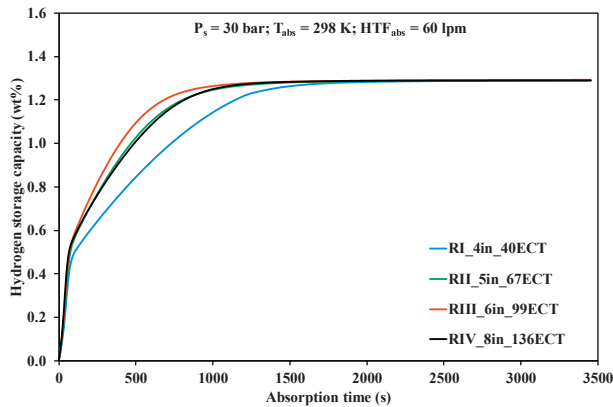


Fig. 11 – Effect of reactor geometry on variation of hydrogen storage capacity.

temperature of this model attains a peak value of 328.6 K and takes 1897 s for it to cool down to 300 K, signifying slower heat transfer. Comparatively, HTF outlet temperature of RII_5in_67ECT requires 33.6% less duration to attain 300 K.

Interestingly, the rate of decrease in HTF outlet temperature of RIV_8in_136ECT is similar to that of RII_5in_67ECT until about 440 s. Beyond this, the rate of decrease is slower due to larger radius of model causing delayed evolution of absorption heat in regions near to the periphery of model. HTF outlet temperature of this model attains a peak value of 323.2 K and requires 1568 s for cooling down to 300 K. Compared to all these models, HTF outlet temperature of RIII_6in_99ECT model attains a peak of 319.5 K which reduced to 300 K within 1001 s. This is a reduction of 47.3% in duration when compared to RI_4in_40ECT. RIII_6in_99ECT shows better heat transfer and is able to liberate the generated heat of absorption faster than other models. This leads to robust absorption which is the ultimate objective of the designed models. Additionally, it can be inferred that increasing the diameter or length of the model beyond the dimensions of these 4 reactor models would further reduce the hydriding performance. Based on the hydriding performance, RIII_6in_99ECT model is selected for further parametric investigations.

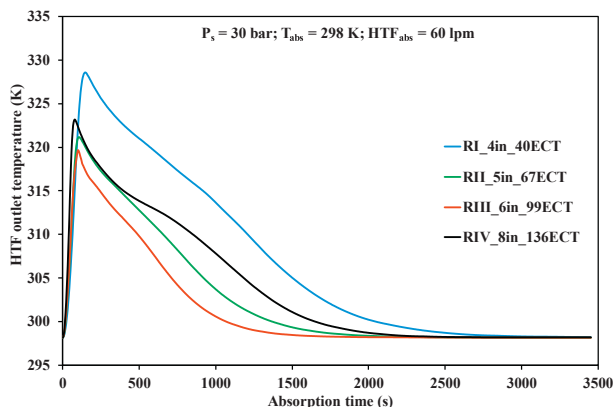


Fig. 12 – Effect of reactor geometry on variation of HTF outlet temperature.

Parametric investigation on RIII_6in_99ECT model

Effect of hydrogen supply pressure (P_s)

In order to understand the effect of varying hydrogen supply pressure (P_s) on T_{Vavg} and HSC, P_s is varied from 5 bar to 35 bar in steps of 5 bar while absorption temperature and water flow rate are maintained at 298 K and 30 lpm, respectively.

As portrayed in Figs. 13 and 14, varying P_s have phenomenal effects on the hydriding rate of RIII_6in_99ECT which contains 50 kg of $\text{LaNi}_{4.7}\text{Al}_{0.3}$. From the absorption reaction rate equation, it is understood that the rate of absorption depends primarily on the pressure gradient between supply pressure (P_s) and equilibrium pressure (P_{eq}). From the volume average bed temperature variation and concentration variation within bed, average equilibrium pressure is estimated considering the complete hydriding reaction. The pressure gradient (P_{grad}) is further estimated based on this average equilibrium pressure and supply pressure. At 5 bar supply pressure, P_{grad} is just 2.9 bar. However, increasing P_s to 10, 15, 20, 25, 30 and 35 bar, respectively leads to P_{grad} of 7.3, 11.4, 15.1, 18.7, 22.4 and 26.1 bar which in turn results in larger driving force for absorption reaction. At P_s of 5 bar, T_{Vavg} attains a peak value of 338.3 K and requires 2720 s for cooling down to 300 K. Meanwhile, it attains a HSC of just 0.72 wt% even after an absorption time of 3450 s, depicting slower reaction kinetics. Increasing supply pressure to 10 bar and 15 bar, respectively yields a HSC of 1.14 wt% and 1.21 wt%. When P_s is further increased to 20 bar, HSC of 1.24 wt% is attained while T_{Vavg} drops from 393 K to 300 K within 2600 s. It can be understood that increase in supply pressure up to 20 bar enhances HSC significantly.

Rapid reaction kinetics can be realized at supply pressure higher than 20 bar, wherein rapid absorption causes T_{Vavg} to attain higher peak value and in turn leads to faster heat transfer. For P_s of 25 bar, HSC is 1.28 wt% and peak value of T_{Vavg} is higher by 19.7 K due to 23.8% increase in P_{grad} when P_s is increased from 20 bar to 25 bar. For this variation in P_s , time taken by T_{Vavg} for dropping down to 300 K reduces by 22%. Further increase in P_s to 30 bar and 35 bar lead to HSC of 1.29 wt%, which demonstrates that P_s of 30 bar facilitates in achieving maximum absorption at the given supply condition. Though the peak T_{Vavg} is 426.2 K at 35 bar which is 5.3 K more than peak T_{Vavg} at 30 bar, both cases cool down to 300 K in about 2200 s depicting similar performance despite 17.9%

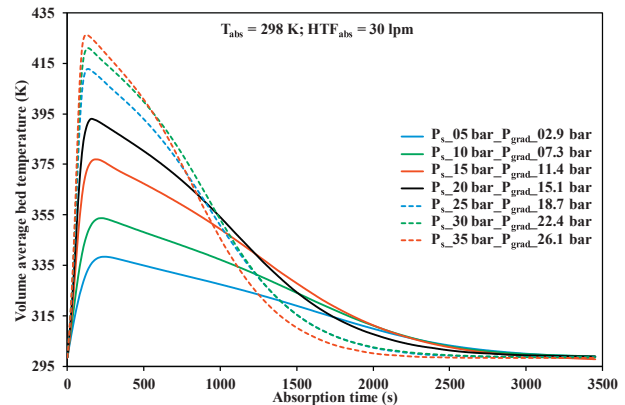


Fig. 13 – Effect of hydrogen supply pressure (P_s) on variation of volume average bed temperature.

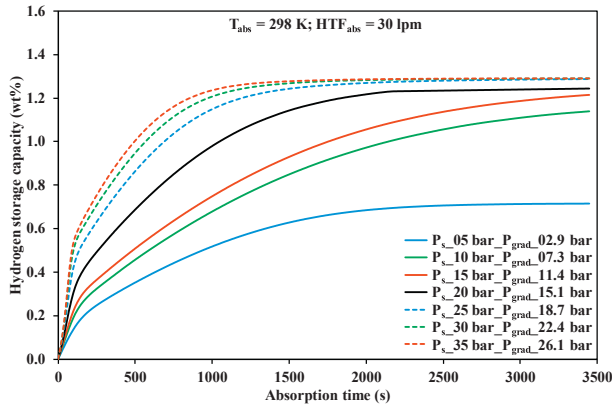


Fig. 14 – Effect of hydrogen supply pressure (P_s) on hydrogen storage capacity.

increase in P_{grad} . This denotes saturation in absorption performance at P_s of 30 bar and hence, it is suitable for absorption of $\text{LaNi}_{4.7}\text{Al}_{0.3}$ in RIII_6in_99ECT.

Effect of absorption temperature (T_{abs})

To understand the effect of varying absorption temperature (T_{abs}) on absorption kinetics, T_{abs} is varied from 293 K to 308 K in steps of 5 K while P_s is maintained at 20 bar and HTF flow rate is at 30 lpm. The absorption temperature is varied among this range considering various naturally available heat sinks and the wide range of driving potential offered by them. The influence of absorption temperature (T_{abs}) on T_{Vavg} and HSC can be respectively presented in Figs. 15 and 16.

Within 160 s, T_{abs} of 308 K causes a peak T_{Vavg} of 394.4 K while, the same is just 2.6 K less for T_{abs} of 293 K. Hence, hydriding rate is nearly same for different T_{abs} during initial phase of reaction (Fig. 16). However, lower T_{abs} triggers slightly larger pressure gradient (P_{grad}) leading to better rate of absorption. Owing to PCT characteristics of the material, average equilibrium pressure of the bed increases from 4.5 bar to 5.8 bar when T_{abs} is correspondingly increased from 293 K to 308 K. For T_{abs} of 293 K, T_{Vavg} of bed drops down to 310 K within 1680 s while the P_{grad} is 15.5 bar. When the T_{abs} is increased to 298 K, 303 K and 308 K, P_{grad} marginally reduces by 2.6%, 5.2% and 8.4%, respectively which in turn caused 8.7%, 33.3% and 66.7% increase in the duration taken by T_{Vavg} of respective bed to attain 310 K. This validates the fact that at lower T_{abs} , P_{grad} is marginally higher leading to better heat transfer characteristics. Though total HSC of 1.24 wt% is achieved in all cases as P_s is 20 bar, hydriding rate is slightly better for T_{abs} of 293 K. Within 560 s, bed has attained a HSC of 0.74 wt% for T_{abs} of 293 K. There is a comparative reduction of 1.1%, 2.6% and 4.5% in HSC attained within 560 s, when T_{abs} is increased respectively to 298 K, 303 K and 308 K. It is apparent that T_{abs} has minimal influence on hydriding rate and HSC. Hence, the absorption of alloy can take place at ambient temperature, as it is less energy intensive to maintain.

Effect of HTF flow rate (HTF_{abs})

The flow rate of HTF (HTF_{abs}) is also one of the parameters that significantly influences the absorption performance of MHHSR. At a higher volumetric flow rate of water, the heat removal is faster which led to larger pressure gradient and

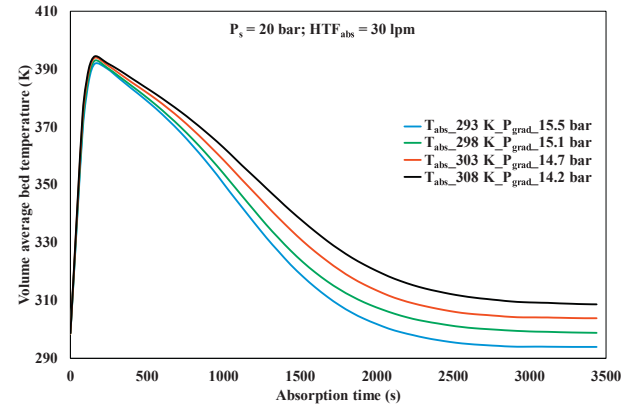


Fig. 15 – Effect of absorption temperature (T_{abs}) on volume average bed temperature variation.

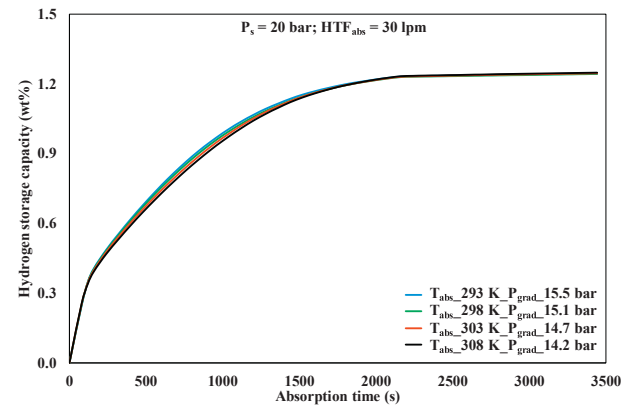


Fig. 16 – Effect of absorption temperature (T_{abs}) on hydrogen storage capacity.

improved rate of absorption. The effect of HTF_{abs} on the T_{Vavg} and HSC are presented in Figs. 17 and 18, respectively. At the absorption condition of 30 bar and 298 K, HTF_{abs} is varied from 10 lpm to 35 lpm in increments of 5 lpm. Within 140 s, a peak T_{Vavg} of 424 K is attained for HTF_{abs} of 10 lpm while for 35 lpm, it is 420.9 K. HTF_{abs} caused minuscule variation on peak T_{Vavg} attained as this temperature primarily depends on supply pressure. On the other hand, the rate of heat transferred from MH bed to HTF is highly influenced by HTF_{abs} which can be observed from the duration required by bed for dropping down to 300 K. The effect of varying HTF_{abs} on the driving potential variation is the cause for such phenomenon. As the supply pressure and absorption temperature are constant for different HTF flow rates, the initial pressure gradient is constant as well. However, variation of T_{Vavg} due to variation in HTF flow rate in turn affects the P_{grad} throughout the reaction as evident from Fig. 17. For HTF_{abs} of 10 lpm, MH bed needs 3450 s to attain 300 K while this duration reduces by 4.9%, 22.7%, 25%, 33.6% and 34.2% when HTF_{abs} is increased to 15, 20, 25, 30 and 35 lpm, respectively. Although the maximum HSC of 1.29 wt% is achieved for different flow rate values, hydriding rate is rapid at higher HTF_{abs} . HSC of 1.03 wt% is achieved within 1020 s when HTF_{abs} is 10 lpm and P_{grad} is 17.6 bar.

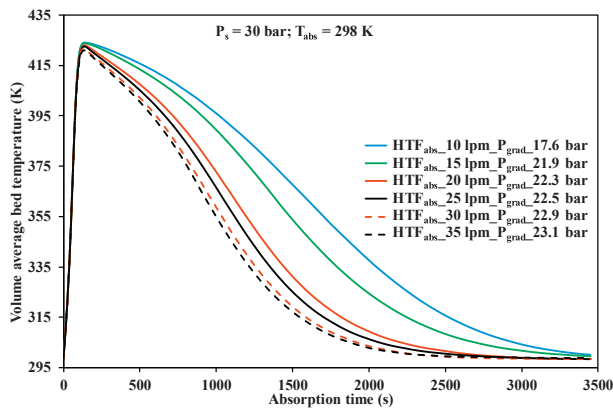


Fig. 17 – Effect of HTF flow rate (HTF_{abs}) on variation of volume average bed temperature.

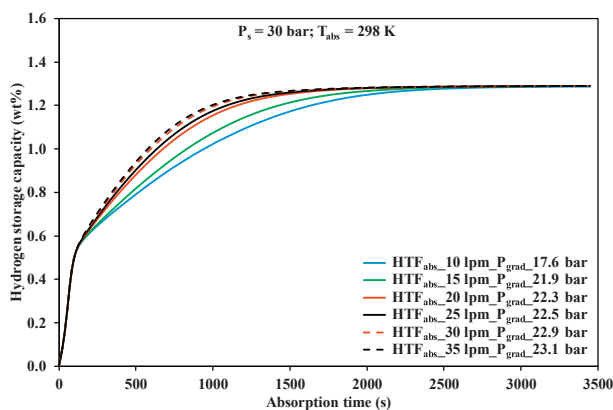


Fig. 18 – Effect of HTF flow rate (HTF_{abs}) on hydrogen storage capacity.

Comparative reduction in absorption time of 11.7% and 28.4% are observed when HTF_{abs} is correspondingly increased to 15 lpm and 20 lpm causing respective increase in P_{grad} to 21.9 bar and 22.3 bar. For HTF_{abs} of 25 lpm, duration of 690 s is required by the MH bed to attain 1.03 wt%. Increasing HTF_{abs} further to 30 lpm and 35 lpm results in achieving 1.03 wt% within 640 s and 620 s, respectively. It can be observed that HTF_{abs} of 30 lpm and 35 lpm portrayed similar hydriding kinetics as their driving potential is nearly equal. Hence, water flow rate of 30 lpm is suitable for hydrogen absorption in RIII_6in_99ECT as it achieves 80% of HSC in 37.3% less duration than at HTF_{abs} of 10 lpm. For an industrial application implementing of this MH storage module, the hydrogen can be supplied in the range of 20–30 bar, while HTF is in the ambient temperature range of 298–308 K with a flow rate of 20–30 lpm.

Conclusions

For designing cylindrical metal hydride based hydrogen storage reactors (MHHSR) with embedded cooling tubes (ECT), a novel set of comprehensive arithmetic correlations have been developed. These correlations facilitate the selection of

cylindrical shell and distribution of ECT within reactor while ensuring uniform bed thickness and balancing the final design against parasitic thermal mass of empty reactor. Following this strategy, cylindrical reactor with ECT can be designed for numerous applications. Based on these correlations, various reactor configurations are designed for holding 50 kg of $LaNi_{4.7}Al_{0.3}$ and using the formulated three dimensional numerical model, hydriding performances of the MHHSR are predicted at a supply condition of 30 bar and 298 K with HTF flow rate of 60 lpm. Reactor with 6 inch nominal diameter shell and 99 ECT (RIII_6in_99ECT) depicts robust hydriding performance achieving total hydrogen storage capacity (HSC) of 1.29 wt%, while 80% of total HSC is attained within 430 s. Using this reactor model, the effects of hydrogen supply pressure (P_s), absorption temperature (T_{abs}) and volumetric water flow rate (HTF_{abs}) on absorption kinetics are predicted in which it is observed that P_s has phenomenal effect followed by HTF_{abs} , while T_{abs} is found to have a minor influence. This variation is due to the influence of operating parameters on the resultant pressure gradient which is the driving potential for the absorption kinetics. At a supply condition of 30 bar, 298 K and 30 lpm water flow rate, total HSC of 1.29 wt% is achieved within 2060 s while the volume average bed temperature (T_{avg}) drops from 420.9 K to 300 K within 2200 s. This is a 120.9 K temperature drop in MH bed of 50 kg. These results corroborate the faster hydriding kinetics of ECT reactor models as well as the ingenuity of developed correlations in designing them for versatile range of capacity and application.

Acknowledgement

The authors express their gratitude to the Ministry of Human Resources and Development (MHRD), Government of India, for the funding (Project No: IMPRINT–Energy-5815).

Appendix A. Supplementary data

Supplementary data to this article can be found online at <https://doi.org/10.1016/j.ijhydene.2019.05.193>.

REFERENCES

- [1] Møller KT, Sheppard D, Ravnsbæk DB, Buckley CE, Akiba E, Li H-W, Jensen TR. Complex metal hydrides for hydrogen, thermal and electrochemical energy storage. *Energies* 2017;10:1645.
- [2] Lototskyy MV, Tolj I, Pickering L, Sita C, Barbir F, Yartys V. The use of metal hydrides in fuel cell applications. *Prog Nat Sci: Mater Int* 2017;27:3–20.
- [3] Fiori C, Dell'Era A, Zuccari F, Santiangeli A, D'Orazio A, Orecchini F. Hydrides for submarine applications: overview and identification of optimal alloys for air independent propulsion maximization. *Int J Hydrogen Energy* 2015;40:11879–89.
- [4] Muthukumar P, Abraham K, Prasad UAR, Maiya MP, Murthy SS. Screening of metal hydrides for engineering applications. In: *Proceedings of 16th international*

- conference on efficiency, cost, optimization, simulation, and environmental impact of energy systems, copenhagen; 2003. p. 93–100.
- [5] Parra D, Gillott M, Walker GS. Design, testing and evaluation of a community hydrogen storage system for end user applications. *Int J Hydrogen Energy* 2016;41:5215–29.
 - [6] Rizzi P, Pinatel E, Luetto C, Florian P, Graizzaro A, Gagliano S, Baricco M. Integration of a PEM fuel cell with a metal hydride tank for stationary applications. *J Alloy Comp* 2015;645:S338–42.
 - [7] Sakintuna B, Darkrim FL, Hirscher M. Metal hydride materials for solid hydrogen storage: a review. *Int J Hydrogen Energy* 2007;32:1121–40.
 - [8] Melnichuk M, Silin N, Peretti HA. Optimized heat transfer fin design for a metal-hydride hydrogen storage container. *Int J Hydrogen Energy* 2009;34:3417–24.
 - [9] Lototskyy MV, Davids MW, Tolj I, Klochko YV, Sekhar BS, Chidziva S, Smith F, Swanepoel D, Pollet BG. Metal hydride systems for hydrogen storage and supply for stationary and automotive low temperature PEM fuel cell power modules. *Int J Hydrogen Energy* 2015;40:11491–7.
 - [10] Lototskyy M, Yartys VA. Comparative analysis of the efficiencies of hydrogen storage systems utilising solid state H storage materials. *J Alloy Comp* 2015;645:S365–73.
 - [11] Muthukumar P, Kumar A, Raju NN, Malleswararao K, Rahman MM. A critical review on design aspects and developmental status of metal hydride based thermal machines. *Int J Hydrogen Energy* 2018;43:17753–79.
 - [12] Karagiorgis G, Christodoulou CN, von Storch H, Tzamalís G, Deligiannis K, Hadjipetrou D, Odysseos M, Roeb M, Sattler C. Design, development, construction and operation of a novel metal hydride compressor. *Int J Hydrogen Energy* 2017;42:12364–74.
 - [13] Sharma VK, Kumar EA. Thermodynamic analysis of novel multi stage multi effect metal hydride based thermodynamic system for simultaneous cooling, heat pumping and heat transformation. *Int J Hydrogen Energy* 2017;42:437–47.
 - [14] Bellosta von Colbe J, Ares J-R, Barale J, Baricco M, Buckley C, Capurso G, Gallandat N, Grant DM, Guzik MN, Jacob I, Jensen EH, Jensen T, Jepsen J, Klassen T, Lototskyy MV, Manickam K, Montone A, Puszkil J, Sartori S, Sheppard DA, Stuart A, Walker G, Webb CJ, Yang H, Yartys V, Zuttel A, Dornheim M. Application of hydrides in hydrogen storage and compression: achievements, outlook and perspectives. *Int J Hydrogen Energy* 2019;44:7780–808.
 - [15] Bhogilla SS, Ito H, Segawa T, Kato A, Nakano A. Experimental study on laboratory scale Totalized Hydrogen Energy Utilization System using wind power data. *Int J Hydrogen Energy* 2017;42:13827–38.
 - [16] Lototskyy M, Tolj I, Klochko Y, Davids MW, Swanepoel D, Linkov V. Metal hydride hydrogen storage tank for fuel cell utility vehicles. *Int J Hydrogen Energy* 2019. <https://doi.org/10.1016/j.ijhydene.2019.04.124>.
 - [17] Muthukumar P, Madhavakrishna U, Dewan A. Parametric studies on a metal hydride based hydrogen storage device. *Int J Hydrogen Energy* 2007;32:4988–97.
 - [18] Mohan G, Maiya MP, Murthy SS. Performance simulation of metal hydride hydrogen storage device with embedded filters and heat exchanger tubes. *Int J Hydrogen Energy* 2007;32:4978–87.
 - [19] Muthukumar P, Satheesh A, Madhavakrishna U, Dewan A. Numerical investigation of coupled heat and mass transfer during desorption of hydrogen in metal hydride beds-A. *Energy Convers Manag* 2009;50:69–75.
 - [20] Satheesh A, Muthukumar P, Dewan A. Computational study of metal hydride cooling system. *Int J Hydrogen Energy* 2009;34:3164–72.
 - [21] Ye J, Jiang L, Li Z, Liu X, Wang S, Li X. Numerical analysis of heat and mass transfer during absorption of hydrogen in metal hydride based hydrogen storage tanks. *Int J Hydrogen Energy* 2010;35:8216–24.
 - [22] Muthukumar P, Maiya MP, Murthy SS. Experiments on a metal hydride-based hydrogen storage device. *Int J Hydrogen Energy* 2005;30:1569–81.
 - [23] Boukhari A, Bessa R. Numerical heat and mass transfer investigation of hydrogen absorption in an annulus-disc reactor. *Int J Hydrogen Energy* 2015;40:13708–17.
 - [24] Muthukumar P, Maiya MP, Murthy SS. Experiments on a metal hydride based hydrogen compressor. *Int J Hydrogen Energy* 2005;30:879–92.
 - [25] Nakano A, Maeda T, Ito H, Motyka T, Perez-Berrios JM, Greenway S. Experimental study on a metal hydride tank for the totalized hydrogen energy utilization system. *Energy Procedia* 2012;29:463–8.
 - [26] Tarasov BP, Bocharnikov MS, Yanenko YB, Fursikov PV, Lototskyy MV. Cycling stability of RNi_5 ($R = La, La+Ce$) hydrides during the operation of metal hydride hydrogen compressor. *Int J Hydrogen Energy* 2018;43:4415–27.
 - [27] Johnson TA, Jorgensen SW, Dedrick DE. Performance of a full-scale hydrogen-storage tank based on complex hydrides. *Faraday Discuss* 2011;151:327–52.
 - [28] Afzal M, Mane R, Sharma P. Heat transfer techniques in metal hydride hydrogen storage: a review. *Int J Hydrogen Energy* 2017;42:30661–82.
 - [29] Singh A, Maiya MP, Murthy SS. Effects of heat exchanger design on the performance of a solid state hydrogen storage device. *Int J Hydrogen Energy* 2015;40:9733–46.
 - [30] Laurencelle F, Goyette J. Simulation of heat transfer in a metal hydride reactor with aluminium foam. *Int J Hydrogen Energy* 2007;32:2957–64.
 - [31] Shaji S, Mohan G. Numerical simulation of the effect of aluminum foam on sorption induced wall strain in vertical, metal hydride based hydrogen storage container. *J Alloy Comp* 2018;735:2675–84.
 - [32] Minko KB, Artemov VI, Yan'kov GG. Numerical study of hydrogen purification using metal hydride reactor with aluminium foam. *Appl Therm Eng* 2015;76:175–84.
 - [33] Miura S, Fujisawa A, Ishida M. A hydrogen purification and storage system using metal hydride. *Int J Hydrogen Energy* 2012;37:2794–9.
 - [34] Krokos CA, Nikolic D, Kikkinides ES, Georgiadis MC, Stubos AK. Modelling and optimization of multi-tubular metal hydride beds for efficient hydrogen storage. *Int J Hydrogen Energy* 2009;34:9128–40.
 - [35] Raju M, Khaitan SK. Charging dynamics of metal hydride hydrogen storage bed for small wind hybrid systems. *Int J Hydrogen Energy* 2011;36:10797–807.
 - [36] Khaitan SK, Raju M. Discharge dynamics of coupled fuel cell and metal hydride hydrogen storage bed for small wind hybrid systems. *Int J Hydrogen Energy* 2012;37:2344–52.
 - [37] Muthukumar P, Singhal A, Bansal GK. Thermal modeling and performance analysis of industrial-scale metal hydride based hydrogen storage container. *Int J Hydrogen Energy* 2012;37:14351–64.
 - [38] Anbarasu S, Muthukumar P, Mishra SC. Thermal modelling of $LaNi_{4.91}Sn_{0.15}$ based solid state hydrogen storage device with embedded cooling tubes. *Int J Hydrogen Energy* 2014;39:15549–62.
 - [39] Mellouli S, Dhaou H, Askri F, Jemni A, Nasrallah SB. Hydrogen storage in metal hydride tanks equipped with metal foam heat exchanger. *Int J Hydrogen Energy* 2009;34:9393–401.
 - [40] Raju M, Kumar S. Optimization of heat exchanger designs in metal hydride based hydrogen storage systems. *Int J Hydrogen Energy* 2012;37:2767–78.

- [41] Askri F, Salah BM, Jemni A, Nasrallah SB. Optimization of hydrogen storage in metal hydride tank. *Int J Hydrogen Energy* 2009;34:897–905.
- [42] Sekhar BS, Lototsky M, Kolesnikov A, Moropeng ML, Tarasov BP, Pollet BG. Performance analysis of cylindrical metal hydride beds with various heat exchange options. *J Alloy Comp* 2015;645:S89–95.
- [43] Wu Z, Yang F, Zhang Z, Bao Z. Magnesium based metal hydride reactor incorporating helical coil heat exchanger: simulation study and optimal design. *Appl Energy* 2014;130:712–22.
- [44] Muthukumar P, Patil MS, Raju NN, Imran Md. Parametric investigations on compressor-driven metal hydride based cooling system. *Appl Therm Eng* 2016;97:87–99.
- [45] Anbarasu S, Muthukumar P, Mishra SC. Tests on $\text{LaNi}_{4.91}\text{Sn}_{0.15}$ based solid state hydrogen storage device with embedded cooling tubes – Part A: absorption process. *Int J Hydrogen Energy* 2014;39:3342–51.
- [46] Anbarasu S, Muthukumar P, Mishra SC. Tests on $\text{LaNi}_{4.91}\text{Sn}_{0.15}$ based solid state hydrogen storage device with embedded cooling tubes – Part B: desorption process. *Int J Hydrogen Energy* 2014;39:4966–72.
- [47] Yang FS, Wang GX, Zhang ZX, Meng XY, Rudolph V. Design of the metal hydride reactors – a review on the key technical issues. *Int J Hydrogen Energy* 2010;35:3832–40.
- [48] Mazzucco A, Dornheim M, Sloth M, Jensen TR, Jensen JO, Rokni M. Bed geometries, fueling strategies and optimization of heat exchanger designs in metal hydride storage systems for automotive applications: a review. *Int J Hydrogen Energy* 2014;39:17054–74.
- [49] Choi H, Mills AF. Heat and mass transfer in metal hydride beds for heat pump applications. *Int J Heat Mass Transf* 1990;33:1281–8.
- [50] Muthukumar P, Umekar MM. Study of coupled heat and mass transfer during absorption of hydrogen in $\text{MmNi}_{4.6}\text{Al}_{0.4}$ based hydrogen storage device. *Sadhana* 2009;34:255–70.
- [51] Chibani A, Bougriou C, Merouani S. Simulation of hydrogen absorption/desorption on metal hydride $\text{LaNi}_5\text{-H}_2$: mass and heat transfer. *Appl Therm Eng* 2018;142:110–7.
- [52] Mayer U, Groll M, Supper W. Heat and mass transfer in metal hydride reaction beds: experimental and theoretical results. *J Less Common Met* 1987;131:235–44.
- [53] Jemni A, Nasrallah SB. Study of two dimensional heat and mass transfer during absorption in a metal hydride reactor. *Int J Hydrogen Energy* 1995;20:43–52.
- [54] Nishizaki T, Miyamoto K, Yoshida K. Coefficient performance of hydride heat pumps. *J Less Common Met* 1983;89:559–66.
- [55] Hahne E, Kallweit J. Thermal conductivity of metal hydride materials for storage of hydrogen: experimental investigation. *Int J Hydrogen Energy* 1998;23:107–14.